



# Deciphering thermal failure mechanism of Sodium-Ion battery with O3-phase layered cathode

Shini Lin<sup>a</sup>, Wei Li<sup>a</sup>, Yuan Qin<sup>a</sup>, Honghao Xie<sup>a</sup>, Xue Li<sup>d</sup>, Jing Zeng<sup>a,\*</sup>, Peng Zhang<sup>b,\*</sup>, Jinbao Zhao<sup>a,c,\*\*</sup> 

<sup>a</sup> State-Province Joint Engineering Laboratory of Power Source Technology for New Energy Vehicle, State Key Laboratory of Physical Chemistry of Solid Surfaces, Engineering Research Center of Electrochemical Technology, Collaborative Innovation Center of Chemistry for Energy Materials, College of Chemistry and Chemical Engineering, Ministry of Education, Xiamen University, Xiamen 361005, China

<sup>b</sup> College of Energy & School of Energy Research, Xiamen University, Xiamen 361102, China

<sup>c</sup> Innovation Laboratory for Sciences and Technologies of Energy Materials of Fujian Province (IKKEM), Xiamen 361005, China

<sup>d</sup> National Local Joint Engineering Research Center for Lithium-ion Batteries and Materials Preparation Technology, Key Laboratory of Advanced Batteries Materials of Yunnan Province, Faculty of Metallurgical and Energy Engineering, Kunming University of Science and Technology, Kunming 650093, China

## ARTICLE INFO

### Keywords:

Thermal runaway  
Structure  
Internal crosstalk  
Heat  
O3-phase layered cathode  
Sodium-ion battery

## ABSTRACT

Sodium-ion batteries assembled with  $\text{NaNi}_{1/3}\text{Fe}_{1/3}\text{Mn}_{1/3}\text{O}_2$  (NFM) cathode and hard carbon (HC) anode, show great application prospect due to their relatively high energy density. However, the NFM cathode is accompanied by poor thermal stability detrimental to battery safety, hindering the real commercial application. Here, the detailed thermal runaway process of NFM/HC cell is systematically dissected from cell, electrode and material levels. On cell level, fully charged NFM/HC pouch cell exhibits thermal runaway hazards when abused, which is further proved in adiabatic conditions. On electrode level, heat during the thermal runaway process is collaboratively supplied by NFM and HC. The HC anode induces the initial heat generation, which roots in the anode-electrolyte interface decomposition as the initial chain reactions accumulating heat and mild temperature rise going to battery thermal runaway. The cathode generates huge heat (2–3 times that of anode) at a higher temperature, providing the majority of heat for the whole thermal runaway process. On this basis, the thermochemical crosstalk between electrodes is uncovered, as reductive gases attacking the NFM cathode at an earlier stage around 120 °C and electrolyte thermally corroding the cathode at higher temperature. On material level, the NFM cathode loses its layered structure and is corroded into smooth particles due to the different internal crosstalk with temperature. The strategies on how to improve the safety from such three levels were also discussed. These findings shed light on the journey of designing safer commercial sodium-ion batteries through a systematic analysis at multiple scales, including batteries, electrodes, and materials.

## 1. Introduction

It is widely believed that sodium-ion batteries (SIBs) have broad prospects in the energy storage market for its widely distributed rich resources, low cost, excellent electrochemical performance and compatibility with the existing manufacturing technology [1–5]. However, SIBs as a typical chemical energy storage device with considerable energy density should also have safety hazards [6–9], especially in large-scale energy storage applications. These safety hazards usually show an

uncontrollable thermal runaway process and could seriously hinder the large-scale application of SIBs. Therefore, establishing a clear insight into its thermal runaway mechanism will provide foundation on how to further research and develop SIBs and improve their safety, which is undoubtedly necessary and urgent for the smooth commercial applications of SIBs.

Among anode materials of SIBs, hard carbon (HC) has become the most potential candidate because of its low voltage plateau, high specific capacity and wide range of raw materials [10–16]. For cathode

\* Corresponding authors.

\*\* Corresponding author at: State-Province Joint Engineering Laboratory of Power Source Technology for New Energy Vehicle, State Key Laboratory of Physical Chemistry of Solid Surfaces, Engineering Research Center of Electrochemical Technology, Collaborative Innovation Center of Chemistry for Energy Materials, College of Chemistry and Chemical Engineering, Ministry of Education, Xiamen University, Xiamen 361005, China.

E-mail addresses: [zengjing@xmu.edu.cn](mailto:zengjing@xmu.edu.cn) (J. Zeng), [pengzhang@xmu.edu.cn](mailto:pengzhang@xmu.edu.cn) (P. Zhang), [jbzhao@xmu.edu.cn](mailto:jbzhao@xmu.edu.cn) (J. Zhao).

<https://doi.org/10.1016/j.cej.2025.160202>

Received 24 December 2024; Received in revised form 16 January 2025; Accepted 1 February 2025

Available online 3 February 2025

1385-8947/© 2025 Elsevier B.V. All rights are reserved, including those for text and data mining, AI training, and similar technologies.

materials, layered transition metal oxide materials ( $\text{Na}_x\text{TMO}_2$ , TM = transition metal) characterizing advantages as high capacity, high voltage and easy production process, has become one of the most competitive choices [17–20].  $\text{NaNi}_{1/3}\text{Fe}_{1/3}\text{Mn}_{1/3}\text{O}_2$  (NFM) has become a basic and mature cathode material after long-term research [21–27], and this Na-rich NFM shows a higher capacity. Thus, the SIBs composed of NFM cathode and HC anode has high capacity and high voltage, catering to the pursuit of high energy density. However, relevant research on its thermal runaway process and detailed mechanism of NFM/HC batteries has been lacking. Though there have been a minority of similar studies so far, their conclusions are mostly scattered, not a systematic framework [28–30]. What's more, the igniter fuse and heat source of NFM/HC battery thermal runaway and the thermal failure mechanism of the NFM cathode are still in a blank, stuck in characterizing the thermal runaway phenomenon without looking into the reasons behind it [31]. Additionally, most of the work is limited to focusing on the thermal stability of battery components at the material level [22,30], and there are still few material-electrode-cell multi-dimensional studies to gain the whole map into the thermal runaway mechanism.

In this work, the thermal runaway (TR) pathway of NFM/HC full battery is analyzed from the cell level, electrode level, and material level. Through the abuse tests, the NFM/HC full battery was found to have the fire hazards of TR, so we further quantitatively analyzed the TR behavior of the battery in an adiabatic environment by accelerating rate calorimeter (ARC), and obtained the whole process of battery self-heating below 100 °C and triggering TR near 175 °C to combustion and explosion. The electrode level is taken as the next base point to explore the interaction between the inside battery components and their feedback on the thermal behaviors. And it is found that the cathode-electrolyte (Ca-Ely) and cathode-anode (Ca-An) thermodynamic systems have the much higher thermal runaway maximum temperature than that of anode-electrolyte (An-Ely). It is obtained that the NFM/HC battery TR is induced by HC anode probably due to SEI decomposition and contributed with the main heat by NFM cathode. Based on the material level, the thermal stability of internal components was analyzed to determine the respective contribution to full battery thermal runaway. The fully sodiated HC anode from pouch cells of several cycles has a lower temperature of thermal decomposition accompanied by heat release, and is the initiator of battery self-heating. Its heat flow is weak and the exothermic reactions distribute in a wide temperature range, which provides enough time to find and take actions to knock down the temperature increasing. However, the fully desodiated NFM cathode has a significantly stronger heat flow (11–12 times) and generates more abundant heat (2–3 times) than HC anode, threatening the battery safety largely. In short, the NFM cathode side supports the main heat for battery TR, causing combustion and explosion. It can be noticed that the cathode thermal failure plays an important role in NFM/HC battery safety, and thus it is correlated with the structure evolution for better analysis and guiding the design of more stable structure. At 200 °C, the cathode maintains a P3 + OP2 phase, almost the same as the initial charged to 4.0 V. While at 300 °C, the (003) lattice plane almost disappears due to ion mixing, declaring the complete structure failure of NFM. Besides, the electrolyte will thermally corrode the surface layer of NFM, changing its morphology from rough surface of secondary particles to smooth surface and increasing its specific surface area. Unfortunately, the cathode will have an earlier thermal failure at 120 °C due to the attacking of the reductive gases generated at the HC anode. These results provide a profound insight into the thermal failure process of layered transition metal oxide cathode, of great value for future design of high thermal stability of layered cathode, electrode-level interaction regulation and process development of safer batteries.

## 2. Experimental methods

### 2.1. Experimental materials

NFM has a tap density of 1.65 g/cm<sup>3</sup> and a specific surface area of 0.97 m<sup>2</sup>/g from Zhejiang Natrium Energy Co., Ltd. HC has a particle size of 5 μm, a true density of 1.47 g/cm<sup>3</sup>, and a specific surface area of 6 m<sup>2</sup>/g from Kuraray Co., Ltd. The structure characterization and capacity measurements of NFM and HC are shown in Fig. S1.

### 2.2. Electrochemical performance test

Electrochemical tests were conducted using Neware battery tester. The design and fabrication parameters of NFM/HC cell were shown in Table S1. All batteries were activated at 0.1C current rate and cycled at 1C current rate, with the voltage range of 1.0 ~ 4.0 V.

### 2.3. Safety tests

All the abuse tests were conducted to the international standards. The nail penetration test was vertically piercing into the middle of the fully charged NFM/HC cell by a steel needle with the diameter of 5 mm at a speed of 25 mm/s and kept still for the observation. The thermal abuse test was heating the cell to 130 °C at the rate of 5 °C/min and holding for 0.5 h in the high-temperature test chamber. The overcharge test was charging the cell to 6 V (1.5 times the charging cut-off voltage) at 1C current rate and observing for 1 h. And the ARC (H.E.L.) test was examining the battery thermal runaway behavior in a “heat-wait-search” mode (from 50 °C calibrated for 40 min, then 5 °C as a rise step which was settled for 20 min and searched for whether self-heating (temperature rate  $\geq 0.02$  °C/min) or not. If so, the ARC would synchronize the ambient temperature of the battery with that of the battery for no heat exchange, giving the battery an adiabatic environment to trace its real thermal runaway process. If not, the ARC would continue to give the battery the “heat-wait-search” mode until the self-heating was detected or reaching the maximum detection temperature.

### 2.4. Partial cell Assembling

A 16-Ah fully charged NFM/HC cell was disassembled in an argon-filled glove box with ceramic scissors. The bare cell was rinsed with dimethyl carbonate solvent and dried fully to remove the residual electrolyte. For the An-Ely and Ca-Ely partial cells, the electrolyte was added by 5 g/Ah coefficient, and the capacity of electrodes kept the same. The Ca-An partial cell was extracted partly from the 16-Ah dried cell and its capacity was the same as that of An-Ely and Ca-Ely.

### 2.5. DSC and TGA-MS measurements

The cathode and anode powder were scraping off from the rinsed and dried electrodes of the 16-Ah cell above. For DSC measurements (STA 449 F3 Jupiter instrument type), the sample was placed into a hermetic steel crucible, purged by argon for half an hour at 35 °C, and heated to 400 °C under the rate of 5 °C/min in argon. For the electrode-electrolyte mixtures, the powder and electrolyte (1 M NaPF<sub>6</sub> in EC/PC/DEC with FEC) were added into a hermetic steel crucible in an equal ratio of 1.0 mg to 1.0 μL. For TGA-MS measurements (SDT 650 + Discovery MS instrument type), the sample was placed into an alumina crucible with a hole, purged for half an hour at 25 °C (to reduce the electrolyte volatilization), and heated to 500 °C under the rate of 5 °C/min in nitrogen. For the mixtures, NFM and HC powder were weighed to the N/P ratio in Table S1. For the NFM-HC-electrolyte mixture, 1.0 μL electrolyte was added in the ratio to 1.0 mg powder.

## 2.6. Heat treatment

Fig. S13 is the flow chart of heat treatment to NFM. The cathode electrodes were cut into small pieces and divided into two batches, one of which was put into a ceramic boat with a lid and transferred from the glove box to tube furnace for heat treatment in argon atmosphere, the other of which soaked with the electrolyte was put into a sealing bottle with a sealing rubber ring, sealed again with aluminium tape, and put into a precision energy-saving electric furnace for heat treatment. After cooling naturally to room temperature, these heated NFM cathode electrodes were transferred to the argon glove box, waiting for further testing. Based on DSC results and ARC results of cathode, the heating temperatures were set to 200 °C and 300 °C, which are the non-occurrence and occurrence of the drastic exothermic reactions.

## 2.7. Morphology and structure measurements

The samples were prepared in an argon glove box, and transferred into the scanning electron microscope (Hitachi TM3030) quickly for the morphology observation with the voltage of 15 kV. For transmission electron microscope (TEM, JEOL JEM-2100plus) measurements, the sample was loaded on a 300-mesh copper screen and observed at the voltage of 200 kV for high-resolution lattice fringes. For XRD measurements, the incident angle is increasing from 0° to 45° (2 $\theta$  from 0° to 90°) with copper target, costing 8 min.

## 3. Results and Discussion

### 3.1. Basic electrochemical Performances of NFM/HC battery

In this study, SIBs were designed and assembled to decipher the thermal failure mechanism, and the detailed battery design parameters are shown in Table S1. In the electrochemical performance testing, the

cylindrical cell still remains 97.9 % capacity with tiny voltage plateau attenuation of 52.7 mV and 28.2 mV after 150 cycles, and the pouch cell exhibits an initial energy density of 140.2 Wh/kg and remains 92.5 % capacity after 150 cycles (Fig. S2-3). These results mean that the batteries have considerable performance for ensuring the reliability of following results.

### 3.2. Fire hazards in NFM/HC full battery

Safety assessment and analysis are prerequisites for battery applications. Especially for SIBs that are expected to be applied to large-scale energy storage, a comprehensive and systematic safety analysis is even more important. In the electrode materials for SIBs, NFM and HC as the current mature active materials have higher specific capacity, so NFM/HC battery relatively meets the pursuit of higher-energy-density SIBs. However, more energy density is accompanied with more fire risks.

Here, based on the prepared NFM/HC batteries above, the safety tests were performed at the full battery level (all batteries have experienced several cycles and been fully charged). In the abuse tests around the machine-electric-thermal inducements under international standards, the NFM/HC batteries exhibit poor safety. In the nail penetration test (Fig. 1a and Fig. S4), with the puncture of the steel needle, the battery voltage suddenly drops to 0 V, and the temperature slowly rises to a short plateau of 127 °C and then sharply rises to the highest temperature of 351.4 °C. To gather more information, a video was recorded during the whole process through a camera open in the front window of the nail penetration tester, as shown in Video S1. At about 88 °C, white smoke flashes out of the pressure relief valve of battery. When reaching the short plateau of 127 °C, smoke becomes more intense, and the voltage slightly rebounds to 1.1 V, which is in connection with the thermal reactions between the cathode and anode. In the overcharge test (Fig. 1b and Fig. S5), the discharged battery was charged at 1C to 6 V (1.5 times the charging cut-off voltage in normal operation), showing a

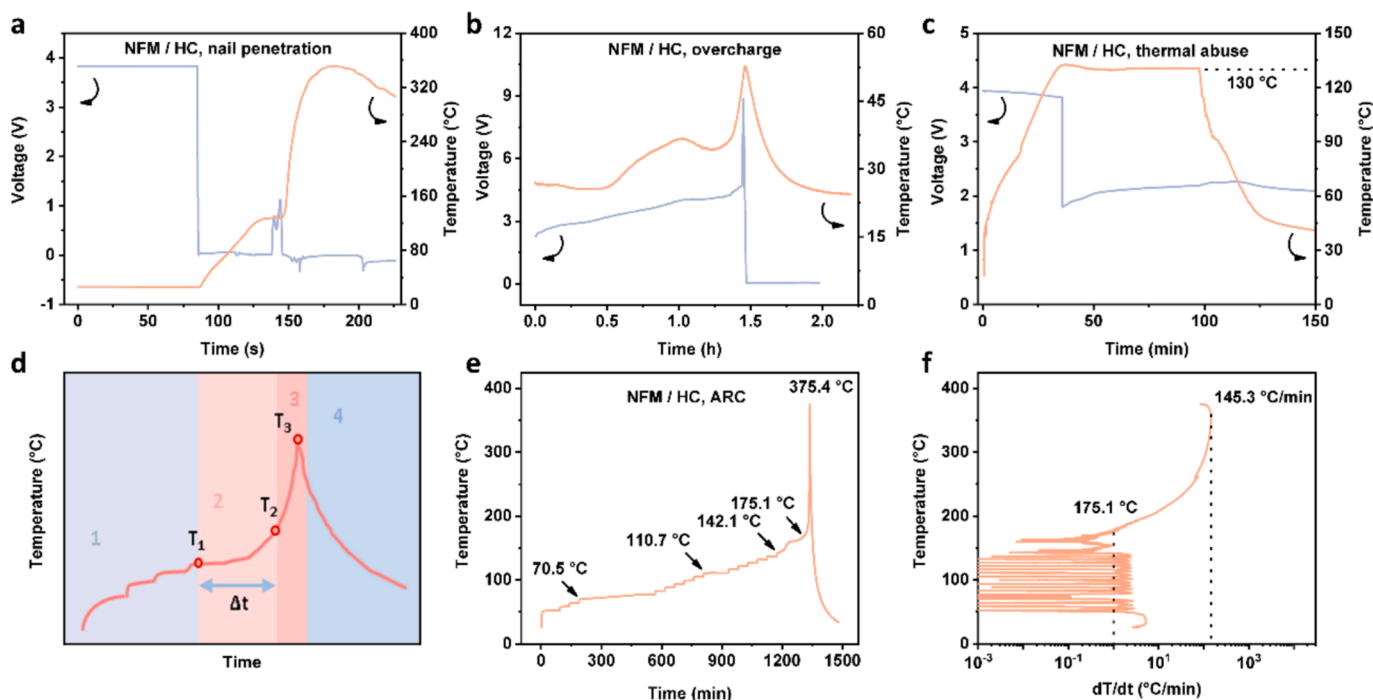


Fig. 1. Safety hazards of NFM/HC batteries (only several cycles). (a-c) Voltage and temperature plots of 1.5-Ah fully charged NFM/HC cell by nail penetration, overcharge and thermal abuse tests respectively. (d) Typical thermal runaway sequence plot of alkali-metal-ion batteries (1: The battery hardly self-generates heat and is relatively safe; 2: The mild temperature rise due to battery self-heating starting with SEI decomposition; 3: The sharp temperature rise and thermal runaway (uncontrollable) due to the violent exothermic reactions usually involving electrolyte or cathode; 4: Termination of thermal runaway, natural cooling down to room temperature.  $\Delta t$ : The reaction time left for salvage precautions when the battery self-heating is detected, which is defined as the time for the mild temperature rise). (e-f) Thermal runaway of 1.5-Ah fully charged NFM/HC cell measured by ARC.

temperature plot of a small peak plus a large peak. The first temperature rise is from the sharp voltage rise, and later the temperature decrease is from the unchanged voltage with the time which the interfacial parasitic reactions temporarily slow down compared with the voltage rise [32]. The first temperature rise and decrease correspond to the temperature peak of 36.7 °C when charged to 4.0 V. The maximum voltage the battery can withstand is 4.7 V, where continuing the voltage will suddenly rise to 8.8 V with the temperature reaching the highest point (52.8 °C), and then drop to 0 V due to an internal short circuit (ISC) with Na metal across the separator from HC anode in the battery [33,34]. In the whole process, the battery does not smoke, fire or explode. In the hot chamber test (Fig. 1c and Fig. S6), as the temperature rises at a rate of 5 °C/min to 130 °C, the battery does not catch fire or explosion. However, its open circuit voltage has dropped from close to 4.0 V to 2.0 V around. Specially, 130 °C is the battery surface temperature rather than the battery internal temperature, so the separator temperature does not reach 130 °C indeed and there is no large-area melting leading to ISC [35]. Thus, the battery voltage will remain at a certain value instead of dropping to 0 V. On the whole, the abuse tests indicate the hazards in NFM/HC battery, which requires further detailed exploration of the TR process.

Therefore, the multi-dimensional safety quantification tests from the overall battery level to the internal electrode level are necessary to analyze the heat source and pathway of NFM/HC battery thermal runaway. ARC, as an important tool to quantify battery safety, can output the characteristic temperatures of battery thermal runaway to suppose the reactions happening inside the battery. These characteristic temperatures are usually expressed as  $T_1$ ,  $T_2$  and  $T_3$  (Fig. 1d) [33,36–38].  $T_1$  is the onset temperature of battery self-heating when the temperature rate reaches 0.02 °C/min, most of which is attributed to the SEI decomposition for LIBs in previous work.  $T_2$  is the TR triggering point when the temperature rate reaches 1 °C/min.  $T_3$  is the maximum temperature during the whole TR process. Between  $T_1$  and  $T_2$ , it is a mild temperature rise accompanied by some reactions with minor heat before the significant threatening exothermic reaction, also the critical time to take salvage precautions and knock down the temperature successfully ( $\Delta t$ ). Starting from  $T_2$ , there is a sharp temperature rise because the fatal chain reactions are triggered, as the uncontrollable and irretrievable fire hazard. Based on the ARC, the TR process of NFM/HC full batteries was further traced and analyzed in an adiabatic environment (Fig. S7). And the measured cell temperature was its surface temperature with the thermocouple attached on the surface. The discharged full cell has no fire or explosion but the melting insulating ring after ARC test (Fig. S8), indicating that there is no thermal runaway in the discharged state. On the contrary, the fully charged NFM/HC cell (109.8 Wh/kg, Fig. S9) has experienced thermal runaway, in particular to multiple  $T_1$  of 70.5 °C, 110.7 °C and 142.1 °C,  $T_2 = 175.1$  °C,  $T_3 = 375.4$  °C and  $(dT/dt)_{\max} = 145.3$  °C/min (the maximum temperature rate of thermal runaway) (Fig. 1e-f). The multistage self-heating processes may be attributed to the thermal decomposition of the SEI and the sodium metal deposited on the HC anode, as well as the exothermic reaction of the electrolyte with the exposed sodiated HC after the SEI decomposition [33,34,39,40]. These reactions lead to the battery discontinuous self-heating behavior. The fully charged NFM/HC cell has fire and explosion as the pressure relief valve punched open and charred electrodes can be seen in the optical image of Fig. S10.

These results prove that NFM/HC battery is not entirely safe, with potential fire and explosion. Therefore, there must be a further understanding of the thermal behaviors of each specific component inside the battery.

### 3.3. TR contribution of partial cells

To analyze the contribution of internal components to battery TR, partial cells of anode-electrolyte (An-Ely), cathode-electrolyte (Ca-Ely), and cathode–anode (Ca-An) thermodynamic systems, were assembled as

shown in Fig. S11 and tested by ARC [41]. The sodiated anode layer has bright white sodium attached to the surface due to the accidental introduction of impurities during cell fabrication process and local gas production during cycling, and the desodiated cathode appears yellow, more mechanically brittle and easily broken than the sodiated NFM cathode (Fig. S12-13). All partial cells have the same electrode layers to guarantee the same capacity.

The An-Ely partial cell initiates self-heating at 119.6 °C and triggers TR at 122.8 °C, going to the maximum temperature of 312.2 °C (Fig. 2a). The Ca-Ely partial cell initiates self-heating at 200.9 °C and triggers TR at 238.7 °C, higher than the An-Ely and Ca-An partial cells (Fig. 2b). However, when it initiates self-heating, violent reactions will happen inside the partial cell and generate a surprisingly high number of calories, taking the partial cell to the maximum temperature higher than 450.6 °C (Fig. S14). Vast gases and impact energy are generated that the aluminum-plastic film shell is completely tore open (Fig. S15), causing that the thermocouple cannot be fixed tight to the partial cell as the temperature turning point in Fig. S14. The Ca-An partial cell initiates self-heating at 121.3 °C and triggers TR at 129.1 °C, going to the maximum temperature of 407.8 °C (Fig. 2c and Fig. S16). It indicates that SEI decomposition brings heat as the beginning of self-heating. When the temperature rises from 121.3 °C to 129.1 °C, the adopted PE separator in accordance with commercial standards begins to melt, causing the anode to directly touch the cathode (Fig. S17). Thus, large joule heat due to the ISC will be generated and bring the partial cell to TR, indicating the thermal runaway trigger mechanism for this battery systems manufactured in accordance with the business model. It can be seen that the maximum temperatures of Ca-Ely and Ca-An partial cells are significantly higher than that of An-Ely partial cell, proving that the cathode is the dominant heat source in the whole thermal runaway process of full battery (Fig. 2d-e).

In conclusion, though the HC anode initiates battery self-heating which is presumably due to SEI decomposition referring to the work of LIBs [33,39,42], the heat generated at the NFM cathode is much larger and more rapid, becoming the more menacing master of battery thermal runaway.

### 3.4. Thermal behaviors of battery components

To deeply analyze the detailed contributions of internal components to battery TR, DSC and thermogravimetric analysis-mass spectrometry (TGA-MS) measurements were conducted to quantitatively evaluate the characteristic thermal behaviors of battery components, including some important node temperatures and heat release.

The charge capacity of NFM and HC from fully charged full cell at 1C is labelled as 113.5 mAh/g and 254.4 mAh/g respectively, related to the active Na content in them. The DSC heat-flow profiles of electrodes are shown in Fig. 3a. For individual materials, sodiated HC has a former exothermic peak at 130.6 °C and the heat flow of 0.36 W/g, which is correlated with SEI decomposition. With the electrolyte added, the former exothermic peak goes ahead to 120.7 °C and the heat flow has little change as 0.32 W/g. The desodiated NFM has a split peak at 285.5 °C and 290.8 °C with heat flow of 1.74 W/g and 1.56 W/g respectively, which is correlated with phase evolution. With the electrolyte added, the exothermic peak goes ahead to 281.3 °C and the heat flow increases to 2.97 W/g due to the exothermic reactions between the electrolyte and the highly-oxidizing-reactive desodiated NFM. It can be seen that the heat flow of cathode is much stronger than the anode. The exothermic reactions of HC anode distribute at such a wide temperature range that there is enough time to intercept. The initial exothermic peak temperature of each component and corresponding heat flow are drawn into a map to indicate the heat source in battery thermal runaway route (Fig. S18). Through integral calculation of the heat flow versus time curves, the heat released by the cathode side is larger than that of the anode side (more than twice, Fig. 3b). The electrolyte has the first exothermic peak at 190.5 °C and the other exothermic peak at 307.6 °C,

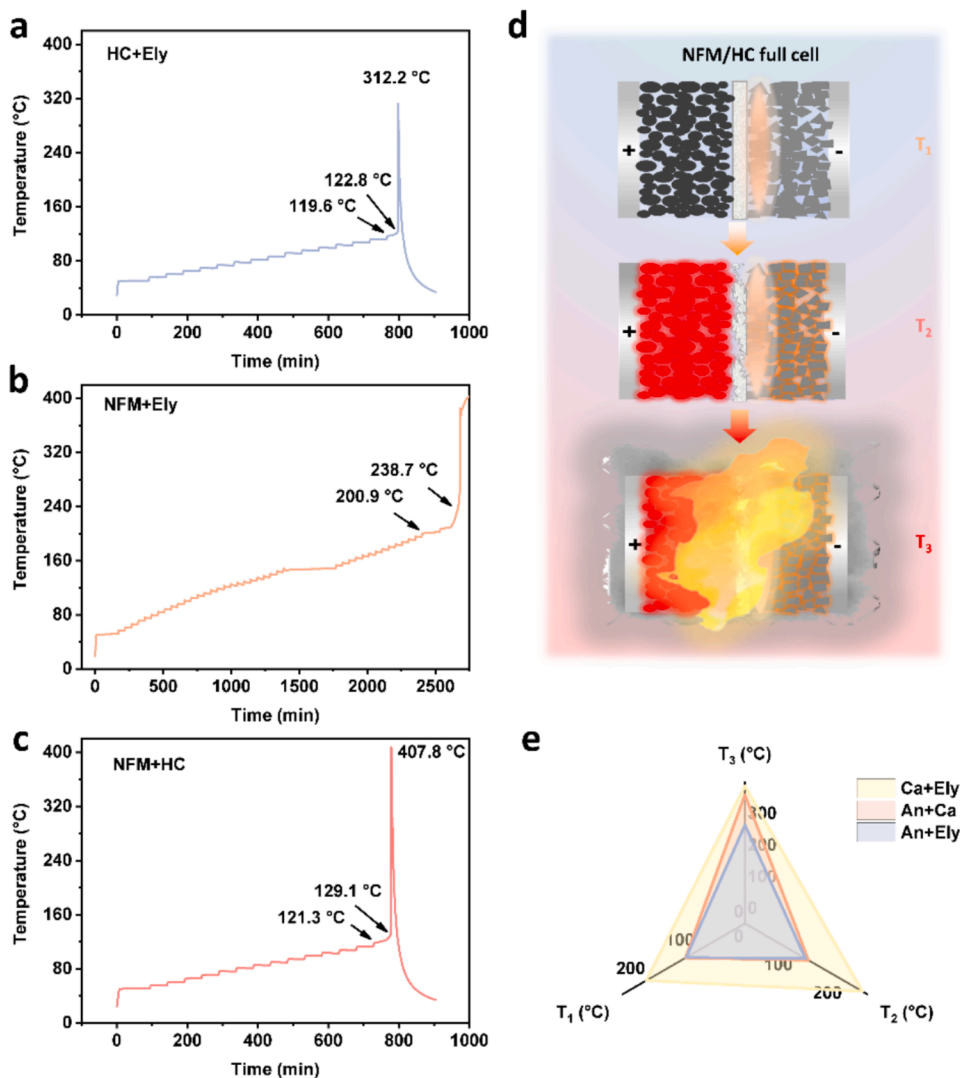


**Fig. 2.** Thermal runaway processes of partial cells. (a) HC anode and electrolyte. (b) NFM cathode and electrolyte. (c) NFM cathode and HC anode. (d) Abridged general view of fully charged NFM/HC battery TR. (e) Critical TR temperatures comparison of three partial cells.

lower than the other two electrolytes, but its heat flow and heat generation are the lowest (Fig. S19-20 and Table S2). Overall, the anode induces the battery self-heating due to its sluggish exothermic reactions at the lower temperature, and the cathode releases the most heat for battery TR due to its abrupt and fierce exothermic reactions at the higher temperature.

The temperature-resolved mass spectrums of NFM-HC mixture and NFM-HC-electrolyte mixture are conducted to understand what gases generate as one of the murderers that bring battery explosion. The NFM-HC mixture produces no  $O_2$ , CO or hydrocarbon compounds ( $CH_x$ ) in the range from RT to 500 °C, while there are two weak and broad  $CO_2$  peaks from 200 °C to 400 °C and more  $CO_2$  released above 415 °C (Fig. 3c). From 200 °C to 400 °C, desodiated NFM releases oxygen, which is mainly reacted to Na in HC. Even if there is some oxygen reacting with HC, produced  $CO_2$  will be consumed by the sodium compounds. Above 400 °C, the reactions of sodium and its compounds are becoming saturated, so there is more oxygen reacting with HC and also less  $CO_2$  is consumed, resulting in the  $CO_2$  curve elevation. The NFM-HC-electrolyte mixture produces no  $O_2$  in the range from RT to 500 °C but  $CO_2$  and the species of  $m/z = 29.00$  (gas-29) in the range from 100 °C to 200 °C (Fig. 3d). The  $CO_2$  generation is speculated to be due to the oxidation of the reductive species such as the electrolyte by the hyper-valent transition metal ions in desodiated NFM. While the gas-29 is

attributed to CO and  $CH_x$  generated at the anode side. It is obvious that the existence of electrolyte will aggravate the battery gas generation with more weight loss over 50 % in a low and narrow temperature range, while the NFM-HC mixture has a smaller weight loss less than 20 % in the full wide range.

From these results, the anode leads to the full cell self-heating, and the cathode is the main source of heat generation, which has a great contribution to battery thermal runaway. Thus, to gain an insight into the specific thermal failure modes of unsafe cathode is crucial for granted, and the concrete effects of the cathode with other battery components during TR need to be clarified.

### 3.5. Postmortem analysis of heat induced structural degradation of NFM cathode

As the cathode generates a largest quantity of heat, which supports most heat during battery thermal runaway, the structural evolution synchronizing with heat generation needs to specify.

To decipher the structural evolution of NFM cathode during TR, desodiated NFM cathode was heated at different temperatures (Fig. S21), and the structure and morphology changes were analyzed. At 200 °C and 300 °C, the desodiated NFM particles have almost no significant morphology changes compared with the initial particles

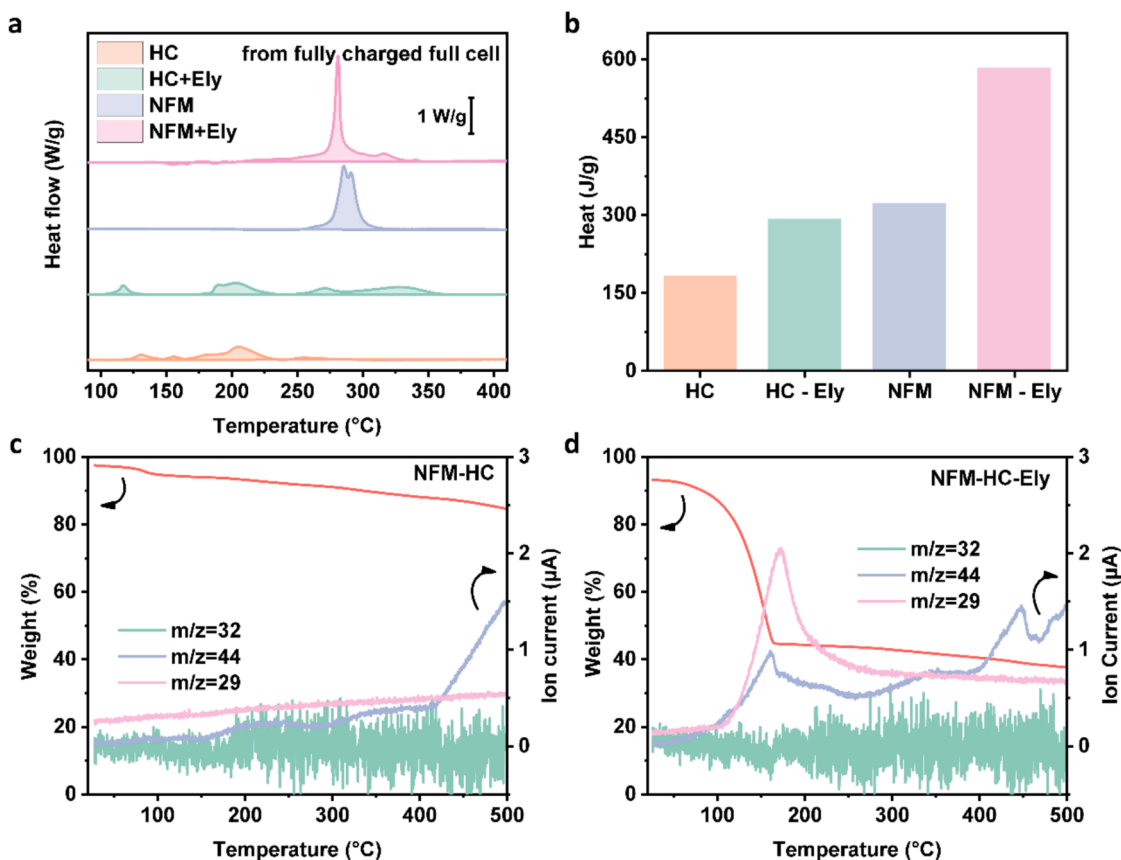


Fig. 3. Thermal behaviors of internal components of fully charged NFM/HC battery. (a-b) Heat flow and heat generation of NFM, HC and electrolyte by DSC measurements. (c) CO<sub>2</sub> and other gas species release of NFM-HC mixture by TGA-MS measurements. (d) CO<sub>2</sub> and other gas species release of NFM-HC-electrolyte mixture by TGA-MS measurements. Ely: electrolyte.

(Fig. 4a, 4b, 4c, 4e and Fig. S22). However, in the presence of electrolyte, heated NFM particles transform into smaller particles with smooth surfaces (Fig. 4d, 4f and Fig. S23). As the temperature increases, the secondary particles become fewer, and smaller smooth spherical particles become more (Fig. 4f). It is speculated that the electrolyte will thermally corrode desodiated NFM cathode, causing the surface region consumed. Further, the thermal corrosion and particle cracking intensification of the electrolyte to NFM cathode are semi quantitatively detected by BET measurements [43]. Compared with NFM heated alone, NFM heated with the electrolyte at 200 °C and 300 °C have more N<sub>2</sub> adsorption/desorption volume and much larger BET specific surface area (> 4 m<sup>2</sup>/g, Fig. 4g-h). This illustrates that the electrolyte will greatly change the shape and size of NFM cathode, which confirms that the electrolyte will thermal corrode the desodiated NFM and cause its more severe thermal failure. Besides, compared with NFM alone, NFM heated with the electrolyte at 300 °C has significant cracks through TEM measurements (Fig. S24). This points out that the electrolyte has dramatically degraded the surface structure of desodiated NFM cathode before the strong exothermic reactions. In the XRD patterns (Fig. 4i), when charged to 4.0 V, a transition from O3 phase to P3 + OP2 phase happens in the NFM structure, with the unit cell volume expands [25,26]. The cathodes heated at 200 °C have almost the same XRD patterns as the initial, indicating its bulk structure stability at 200 °C, and further validating the DSC and ARC results of the cathode thermal stability below 200 °C. With the temperature rise, (003) peak of desodiated NFM significantly weakens and even disappears with the electrolyte existing at 300 °C, marking the layered structural failure. From the critical parameters of (003) peaks at different states listed in Table S3, the  $I_{(003)}/I_{(105)}$  decreases when the temperature rises. From the high-resolution lattice fringe images by TEM (Fig. 4j), there is ion mixing

in NFM particles when heated at 300 °C, which well explains the XRD results. Thus, the complete failure of cathode at 300 °C is not only due to the oxygen release but also the harmful ion mixing. Through low-magnification morphology images by TEM (Fig. S24), there is new phase at 300 °C due to the ion mixing in NFM structure and it cannot fully return to the layered phase when cooling down to RT.

As a whole, the high temperature as 300 °C will cause the desodiated NFM structure failure for the exothermic reactions and ion mixing, and the existence of the electrolyte will thermally corrode its surface region to smaller smooth spherical particles and increase the heat release, confirming that the electrolyte instead of temperature is the dominant role to thermally degrading the surface structure of NFM particles.

### 3.6. Earlier thermal failure of NFM cathode for reductive gas attacking

Above 200 °C, NFM cathode will have exothermic reactions with the electrolyte, providing great heat for battery TR. During the temperature range of separator melting, the cathode will contact with the anode, generating generous joule heat to bring battery TR. These will cause thermal failure to NFM. To clarify whether the cathode will have earlier failure before the battery thermal runaway is triggered, the gases generation at the anode side and its impact on the cathode were analyzed.

According to the An-Ely thermodynamic system with the exothermic peak at 120.7 °C by DSC and the T<sub>1</sub>, T<sub>2</sub> around 120 °C by ARC, HC-Ely partial cells were assembled and heated at 120 °C, 100 °C and 80 °C for the same time to produce reductive gases that will threaten battery safety. The An-Ely partial cells heated at 100 °C and 80 °C do not generate significant gas, indicating the relative thermal stability below 100 °C (Fig. S25). While that heated at 120 °C generates significant gas, which is composed of most C<sub>3</sub>H<sub>6</sub> and C<sub>2</sub>H<sub>4</sub>, and a little C<sub>2</sub>H<sub>6</sub> and H<sub>2</sub> by

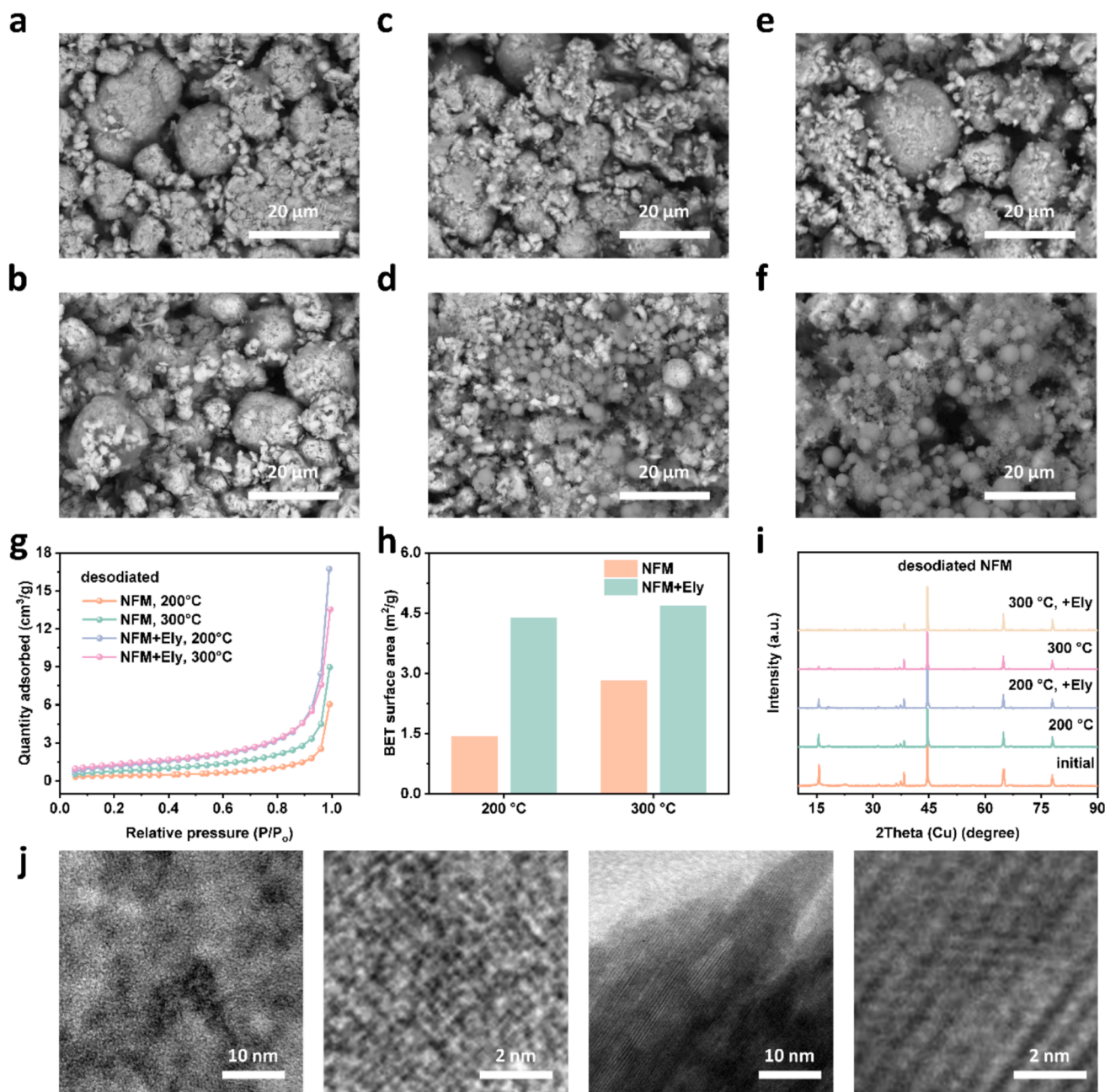


**Fig. 4.** Structural degradation of heated desodiated NFM cathode. (a-b) Surface and cross-sectional morphology of initial desodiated NFM cathode at RT. (c-d) Cross-sectional morphology of desodiated NFM cathode heated at 200 °C alone and with the electrolyte respectively. (e-f) Cross-sectional morphology of desodiated NFM cathode heated at 300 °C alone and with the electrolyte. (g) N<sub>2</sub> adsorption/desorption isotherms and (h) BET specific area of heated desodiated NFM cathode by BET measurements. (i) XRD patterns of initial and heated NFM cathode with/without the electrolyte. (j) High-resolution lattice fringe images of desodiated NFM heated at 300 °C alone (the first two) and with the electrolyte (the last two).

GC measurements, named reductive gases (RG) (Fig. 5a). Injected with the RG, the cathode was heated at 120 °C too (NFM-RG). Through XRD measurements, the (003) peak of NFM-RG has almost disappeared compared with the initial (Fig. 5c). And more than 90 % of NFM-RG gas through postmortem measurements is CO<sub>2</sub>, demonstrating the thermal reactions between the cathode and reductive gases (Fig. 5b). [44] Besides, the morphology of NFM has changed from quasi-spherical surface to flatter surface, with less-content and more unevenly distributed O (Fig. S26). To ensure the rigor, the cathode was also heated at 120 °C alone and with the electrolyte, both not generate significant gas (Fig. S25). And their XRD patterns are almost the same as the initial, with (003) peak existing (Fig. 5c).

Therefore, the reductive gases generated at the anode side will cause

a severe persecution to NFM cathode, making the cathode thermal failure at an early age during battery TR. And the damage mechanism of RG to NFM is shown in Fig. 5d.

To enhance the safety of NFM/HC batteries manufactured to commercial standards based on the TR mechanism and pathway above, corresponding strategies based on battery-electrode-material levels are recommended (Fig. 6).

On battery level, the nail-penetration abuse test difficult to pass hints the major safety risk that cannot be ignored in this type of batteries, mainly affecting T<sub>1</sub> and T<sub>2</sub> during battery thermal runaway as specified in an adiabatic environment for 70.5 °C and 175.1 °C by ARC. The relevant improvement strategies on this level are adjusting the N/P ratio to prevent the production of reductive gases on the anode, and using

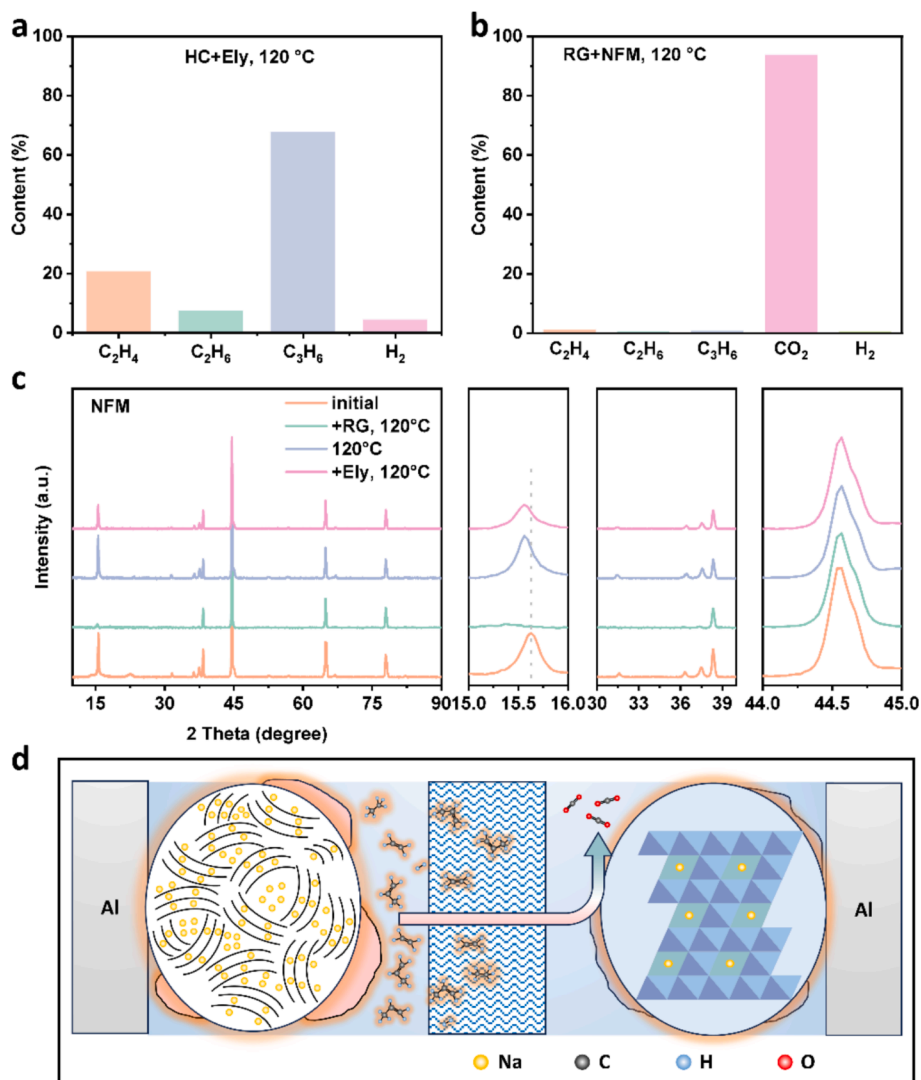


Fig. 5. Reductive gases from HC anode attacking NFM cathode. Gas composition of (a) HC-Ely and (b) NFM-RG partial cells heated at 120 °C through GC measurements. (c) Overall and local XRD patterns of initial and processed NFM. (d) The mechanism schematic diagram of RG to desodiated NFM. RG: reductive gases.

optimized separator to suppress the contact between cathode and anode [33]. On electrode level, the thermal runaway of NFM/HC batteries is induced by the heat release of HC anode presumably due to SEI decomposition, triggered by large joule heat due to PE separator shrinkage, and brought to the highest temperature by the major heat contribution of the NFM cathode. Meanwhile, the reductive gases generated at the HC anode mainly of alkane compounds will attack the NFM cathode causing its earlier failure at 120 °C, and the electrolyte will thermally corrode the cathode at a higher temperature reflected by the stronger and narrower DSC peak. The relevant improvement strategies on this level are recommended as reasonably designing the electrode structure with increased porosity and surface area (for better infiltration and local heat dissipation), and optimizing the electrolyte (for better thermal-stable SEI to delay the thermal runaway process between  $T_1$  and  $T_2$  and reducing the interaction with NFM cathode to reduce the heat generation for TR)[45]. Finally, on material level, the morphology and structure of NFM cathode during thermal failure process caused by various factors are explored to better understand the large heat contribution. The reductive gases generated at the HC anode and the high temperature to 300 °C will invalidate the layered structure of NFM cathode through aggravating the ion mixing, while the electrolyte will thermally corrode the NFM cathode making it smaller and smoother particles. The relevant improvement strategy on this level is enhancing

the material stability, such as phosphate coating layer (which is stable and protective to isolate the attack on electrode level with no negative influence on material electrochemical performance) and monocrystal structure (which is more thermal-stable and less oxygen-release).

#### 4. Conclusions

In this work, the thermal runaway mechanism of SIBs (NFM/HC) and the thermal failure mode of NFM cathode are analyzed from the battery, electrode and material dimensions. From the thermal runaway research, the anode-electrolyte thermodynamic system has a lower self-heating temperature ( $T_1 = 119.6$  °C), and the cathode side has a much higher thermal runaway maximum temperature ( $T_3 > 400$  °C), revealing the thermal runaway mechanism of the HC-electrolyte part generating heat and inducing the full battery thermal runaway, and subsequently the NFM-electrolyte part massively supplying heat to bring the full battery to higher temperature, combustion and explosion. For the poor thermal stability of NFM cathode, we further analyzed its thermal failure modes, containing the thermal corrosion effect of the electrolyte and the thermal attack phenomenon of the reductive gases generated at the HC anode to the NFM cathode. Studies found that the electrolyte will thermally erode the desodiated NFM shell layer (changing the morphology of cathode from secondary-particle rough surfaces to

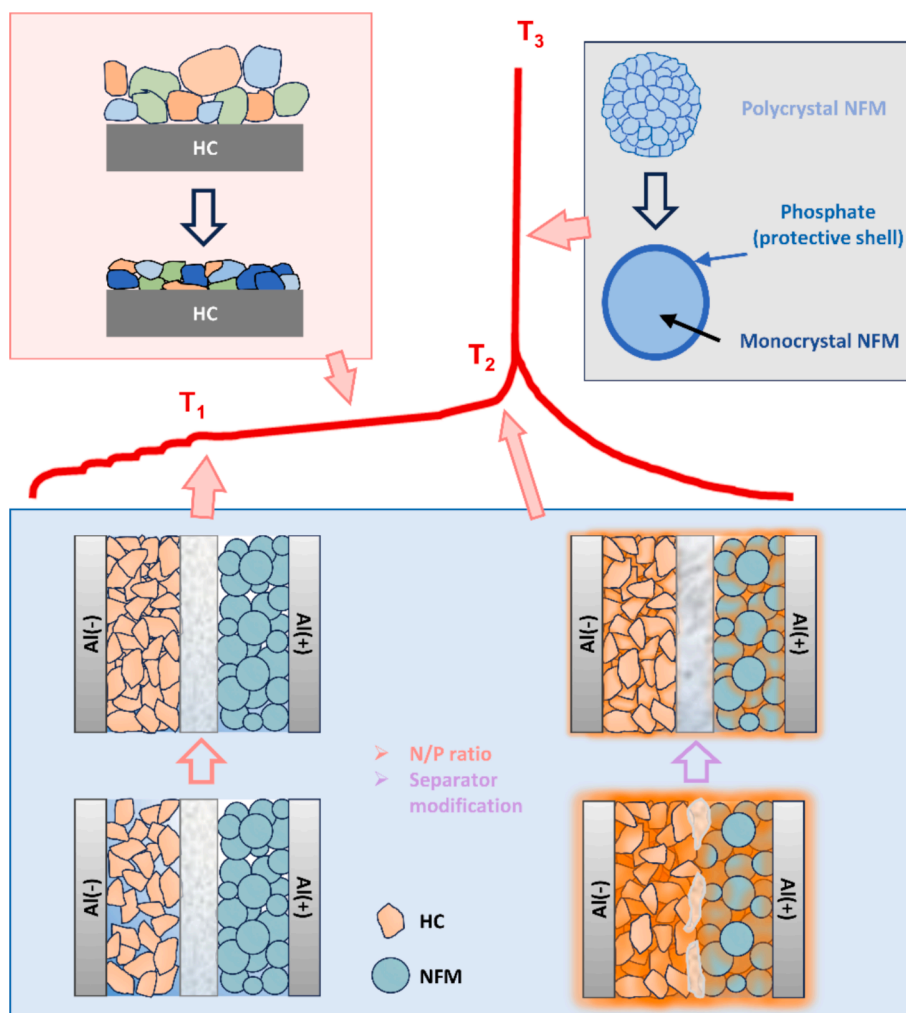


Fig. 6. Cell-electrode-material tri-dimension strategies for the thermal runaway mechanism of NFM/HC batteries.

smooth surfaces and enlarging the specific surface area to 2–4 times) increasing the released heat of cathode, and the reductive gases generated at the HC anode can cause the cathode to lose its layered structure only at 120 °C meaning an earlier thermal failure. To settle and improve, strategies are provided from the three levels respectively, adjusting the N/P ratio and adopting modified separator on the cell level, designing the electrode structure with more porosity and adjusting the interaction between electrodes (SEI construction and Ca-Ely redox reaction inhibition) on the electrode level, and enhancing the thermal stability of layered cathode on the material level. This work systematically explores the thermal runaway of SIBs, conducts the detailed thermal failure analysis to NFM from individual to the chemical crosstalk between battery components, and points out the direction of improvement, which has a clear instructive significance for the development of safer SIBs.

#### CRedit authorship contribution statement

**Shini Lin:** Writing – original draft, Formal analysis, Data curation, Conceptualization. **Wei Li:** Writing – review & editing, Formal analysis. **Yuan Qin:** Investigation. **Honghao Xie:** Investigation. **Xue Li:** Resources, Funding acquisition. **Jing Zeng:** Writing – review & editing, Conceptualization. **Peng Zhang:** Writing – review & editing, Funding acquisition, Conceptualization. **Jinbao Zhao:** Writing – review & editing, Resources, Funding acquisition, Conceptualization.

#### Declaration of competing interest

The authors declare that they have no known competing financial interests or personal relationships that could have appeared to influence the work reported in this paper.

#### Acknowledgements

The authors gratefully acknowledge financial support from the National Key Research and Development Program of China [2021YFB2400300], Yunnan Natural Science Foundation Project [202202AG050003] and National Natural Science Foundation of China [22021001]. And we are grateful to Tan Kah Kee Innovation Laboratory (IKKEM) for help with TGA-MS and TEM measurements.

#### Appendix A. Supplementary data

Supplementary data to this article can be found online at <https://doi.org/10.1016/j.cej.2025.160202>.

#### Data availability

Data will be made available on request.

## References

- [1] Y. Gao, H. Zhang, J. Peng, L. Li, Y. Xiao, L. Li, Y. Liu, Y. Qiao, S.-L. Chou, A 30-year overview of sodium-ion batteries, *Carbon Energy* 6 (2024) e464.
- [2] C. Vaalma, D. Buchholz, M. Weil, S. Passerini, A cost and resource analysis of sodium-ion batteries, *Nat Rev Mater* 3 (2018) 1–11, <https://doi.org/10.1038/natrevmats.2018.13>.
- [3] H.S. Hirsh, Y. Li, D.H.S. Tan, M. Zhang, E. Zhao, Y.S. Meng, Na-Ion Batteries: Sodium-Ion Batteries Paving the Way for Grid Energy Storage (*Adv. Energy Mater.* 32/2020), *Advanced Energy Materials* 10 (2020) 2070134. 10.1002/aenm.202070134.
- [4] J.-Y. Hwang, S.-T. Myung, Y.-K. Sun, Sodium-ion batteries: present and future, *Chem. Soc. Rev.* 46 (2017) 3529–3614, <https://doi.org/10.1039/C6CS00776G>.
- [5] D. Hou, D. Xia, E. Gabriel, J.A. Russell, K. Graff, Y. Ren, C.-J. Sun, F. Lin, Y. Liu, H. Xiong, Spatial and Temporal Analysis of Sodium-Ion Batteries, *ACS Energy Lett.* 6 (2021) 4023–4054, <https://doi.org/10.1021/acseenergylett.1c01868>.
- [6] T. Wei, X.-L. Xian, S.-X. Dou, W. Chen, S.-L. Chou, Comprehensive analysis and mitigation strategies for safety issues of sodium-ion batteries, *Rare Met.* 43 (2024) 1343–1349, <https://doi.org/10.1007/s12598-023-02347-4>.
- [7] Y. Li, Y. Lu, L. Chen, Y.-S. Hu, Failure analysis with a focus on thermal aspect towards developing safer Na-ion batteries\*, *Chinese Phys. B* 29 (2020) 048201, <https://doi.org/10.1088/1674-1056/ab7906>.
- [8] C. Yang, S. Xin, L. Mai, Y. You, Materials Design for High-Safety Sodium-Ion Battery, *Adv. Energy Mater.* 11 (2021) 2000974, <https://doi.org/10.1002/aenm.202000974>.
- [9] Y. Wang, R. Ou, J. Yang, Y. Xin, P. Singh, F. Wu, Y. Qian, H. Gao, The safety aspect of sodium ion batteries for practical applications, *Journal of Energy, Chemistry* 95 (2024) 407–427, <https://doi.org/10.1016/j.jechem.2024.03.060>.
- [10] L. Li, Y. Zheng, S. Zhang, J. Yang, Z. Shao, Z. Guo, Recent progress on sodium ion batteries: potential high-performance anodes, *Energy Environ. Sci.* 11 (2018) 2310–2340, <https://doi.org/10.1039/C8EE01023D>.
- [11] N. LeGe, X.-X. He, Y.-X. Wang, Y. Lei, Y.-X. Yang, J.-T. Xu, M. Liu, X. Wu, W.-H. Lai, S.-L. Chou, Reappraisal of hard carbon anodes for practical lithium/sodium-ion batteries from the perspective of full-cell matters, *Energy Environ. Sci.* 16 (2023) 5688–5720, <https://doi.org/10.1039/D3EE02202A>.
- [12] H. Sun, Q. Zhang, Y. Ma, Z. Li, D. Zhang, Q. Sun, Q. Wang, D. Liu, B. Wang, Unraveling the mechanism of sodium storage in low potential region of hard carbons with different microstructures, *Energy Storage Mater.* 67 (2024) 103269, <https://doi.org/10.1016/j.ensm.2024.103269>.
- [13] R. Dong, L. Zheng, Y. Bai, Q. Ni, Y. Li, F. Wu, H. Ren, C. Wu, Elucidating the Mechanism of Fast Na Storage Kinetics in Ether Electrolytes for Hard Carbon Anodes, *Adv. Mater.* 33 (2021) 2008810, <https://doi.org/10.1002/adma.202008810>.
- [14] X. Feng, Y. Li, Y. Li, M. Liu, L. Zheng, Y. Gong, R. Zhang, F. Wu, C. Wu, Y. Bai, Unlocking the local structure of hard carbon to grasp sodium-ion diffusion behavior for advanced sodium-ion batteries, *Energy Environ. Sci.* 17 (2024) 1387–1396, <https://doi.org/10.1039/D3EE03347C>.
- [15] M. Liu, F. Wu, Y. Gong, Y. Li, Y. Li, X. Feng, Q. Li, C. Wu, Y. Bai, Interfacial-Catalysis-Enabled Layered and Inorganic-Rich SEI on Hard Carbon Anodes in Ester Electrolytes for Sodium-Ion Batteries, *Adv. Mater.* 35 (2023) 2300002, <https://doi.org/10.1002/adma.202300002>.
- [16] Z. Wang, X. Feng, Y. Bai, H. Yang, R. Dong, X. Wang, H. Xu, Q. Wang, H. Li, H. Gao, C. Wu, Probing the Energy Storage Mechanism of Quasi-Metallic Na in Hard Carbon for Sodium-Ion Batteries, *Adv. Energy Mater.* 11 (2021) 2003854, <https://doi.org/10.1002/aenm.202003854>.
- [17] S. Chu, S. Guo, H. Zhou, Advanced cobalt-free cathode materials for sodium-ion batteries, *Chem. Soc. Rev.* 50 (2021) 13189–13235, <https://doi.org/10.1039/D1CS00442E>.
- [18] B. Peng, Z. Zhou, J. Shi, X. Huang, Y. Li, L. Ma, Earth-Abundant Fe-Mn-Based Compound Cathodes for Sodium-Ion Batteries: Challenges and Progress, *Adv. Funct. Mater.* 34 (2024) 2311816, <https://doi.org/10.1002/adfm.202311816>.
- [19] G.-L. Xu, R. Amine, Y.-F. Xu, J. Liu, J. Gim, T. Ma, Y. Ren, C.-J. Sun, Y. Liu, X. Zhang, S.M. Heald, A. Solhy, I. Saadoun, W.L. Mattis, S.-G. Sun, Z. Chen, K. Amine, Insights into the structural effects of layered cathode materials for high voltage sodium-ion batteries, *Energy Environ. Sci.* 10 (2017) 1677–1693, <https://doi.org/10.1039/C7EE00827A>.
- [20] Y. Zhao, Q. Liu, X. Zhao, D. Mu, G. Tan, L. Li, R. Chen, F. Wu, Structure evolution of layered transition metal oxide cathode materials for Na-ion batteries: Issues, mechanism and strategies, *Mater. Today* 62 (2023) 271–295, <https://doi.org/10.1016/j.mattod.2022.11.024>.
- [21] C. Jiang, Y. Wang, Y. Xin, Q. Zhou, Y. Pang, B. Chen, Z. Wang, H. Gao, A high-rate and air-stable cathode material for sodium-ion batteries: yttrium-substituted O3-type Ni/Fe/Mn-based layered oxides, *J. Mater. Chem. A* 12 (2024) 13915–13924, <https://doi.org/10.1039/D4TA01852D>.
- [22] Y. Gan, P. Ping, J. Wang, Y. Song, W. Gao, Comparative analysis of thermal stability and electrochemical performance of NaNi1/3Fe1/3Mn1/3O2 cathode in different electrolytes for sodium ion batteries, *J. Power Sources* 594 (2024) 234008, <https://doi.org/10.1016/j.jpowsour.2023.234008>.
- [23] L. Dai, Z. Guo, Z. Wang, S. Xu, S. Wang, W. Li, G. Zhang, Y.-J. Cheng, Y. Xia, Defensive and Ion Conductive Surface Layer Enables High Rate and Durable O3-type NaNi1/3Fe1/3Mn1/3O2 Sodium-Ion Battery Cathode, (n.d.). 10.1002/smll.202305019.
- [24] H. Yang, D. Wang, Y. Liu, Y. Liu, B. Zhong, Y. Song, Q. Kong, Z. Wu, X. Guo, Improvement of cycle life for layered oxide cathodes in sodium-ion batteries, *Energy Environ. Sci.* 17 (2024) 1756–1780, <https://doi.org/10.1039/D3EE02934D>.
- [25] Y. Xie, H. Wang, G. Xu, J. Wang, H. Sheng, Z. Chen, Y. Ren, C.-J. Sun, J. Wen, J. Wang, D.J. Miller, J. Lu, K. Amine, Z.-F. Ma, In Operando XRD and TXM Study on the Metastable Structure Change of NaNi1/3Fe1/3Mn1/3O2 under Electrochemical Sodium-Ion Intercalation, *Adv. Energy Mater.* 6 (2016) 1601306, <https://doi.org/10.1002/aenm.201601306>.
- [26] M. Jeong, H. Lee, J. Yoon, W.-S. Yoon, O3-type NaNi1/3Fe1/3Mn1/3O2 layered cathode for Na-ion batteries: Structural evolution and redox mechanism upon Na (de) intercalation, *J. Power Sources* 439 (2019) 227064, <https://doi.org/10.1016/j.jpowsour.2019.227064>.
- [27] T. Song, Q. Zhang, Y. Chen, P. Zhu, E. Kendrick, Synthesis and design of NaNi1/3Fe1/3Mn1/3O2 cathode materials for long-life sodium-ion batteries, *Chemical Engineering Journal Advances* 16 (2023) 100572, <https://doi.org/10.1016/j.cej.2023.100572>.
- [28] Q. Zhou, Y. Li, F. Tang, K. Li, X. Rong, Y. Lu, L. Chen, Y.-S. Hu, Thermal Stability of High Power 26650-Type Cylindrical Na-Ion Batteries, *Chinese Phys. Lett.* 38 (2021) 076501, <https://doi.org/10.1088/0256-307X/38/7/076501>.
- [29] X. Yang, H. Chen, K. Yang, C. Pan, X. Liao, Z. Ma, Evaluation of safety performance and thermal stability of hard carbon anode for sodium-ion battery, *Chin. J. Process. Eng.* 22 (2022) 552–560.
- [30] R.R. Samigullin, O.A. Drozhzhin, E.V. Antipov, Comparative Study of the Thermal Stability of Electrode Materials for Li-Ion and Na-Ion Batteries, *ACS Appl. Energy Mater.* 5 (2022) 14–19, <https://doi.org/10.1021/acsaem.1c03151>.
- [31] Y. Xie, G.-L. Xu, H. Che, H. Wang, K. Yang, X. Yang, F. Guo, Y. Ren, Z. Chen, K. Amine, Z.-F. Ma, Probing Thermal and Chemical Stability of NaNi1/3Fe1/3Mn1/3O2 Cathode Material toward Safe Sodium-Ion Batteries, *Chem. Mater.* 30 (2018) 4909–4918, <https://doi.org/10.1021/acs.chemmater.8B00047>.
- [32] X. Guo, S. Guo, C. Wu, J. Li, C. Liu, W. Chen, Intelligent Monitoring for Safety-Enhanced Lithium-Ion/Sodium-Ion Batteries, *Adv. Energy Mater.* 13 (2023) 2203903, <https://doi.org/10.1002/aenm.202203903>.
- [33] X. Feng, D. Ren, X. He, M. Ouyang, Mitigating Thermal Runaway of Lithium-Ion Batteries, *Joule* 4 (2020) 743–770, <https://doi.org/10.1016/j.joule.2020.02.010>.
- [34] Q. Gui, B. Xu, K. Yu, X. Wang, J. Li, Y. Xie, R. Yu, X. Zhou, L. Mao, Comparison of NaNi1/3Fe1/3Mn1/3O2 and Na4Fe3(PO4)2(P2O7) cathode sodium-ion battery behavior under overcharging induced thermal runaway, *Chem. Eng. J.* 497 (2024) 154732, <https://doi.org/10.1016/j.cej.2024.154732>.
- [35] L. Peng, X. Kong, H. Li, X. Wang, C. Shi, T. Hu, Y. Liu, P. Zhang, J. Zhao, A Rational Design for a High-Safety Lithium-Ion Battery Assembled with a Heatproof-Fireproof Bifunctional Separator, *Adv. Funct. Mater.* 31 (2021) 2008537, <https://doi.org/10.1002/adfm.202008537>.
- [36] L. Zhao, J. Hou, X. Feng, J. Xu, C. Xu, H. Wang, H. Liu, B. Hou, X. Rui, Y. Gu, L. Lu, C. Bao, M. Ouyang, The trade-off characteristic between battery thermal runaway and combustion, *Energy Storage Mater.* 69 (2024) 103380, <https://doi.org/10.1016/j.ensm.2024.103380>.
- [37] W. Li, H. Li, J. Liu, S. Lin, Q. Chen, W. Ji, Z. He, P. Zhang, J. Zhao, Systematic safety evaluation of quasi-solid-state lithium batteries: a case study, *Energy Environ. Sci.* 16 (2023) 5444–5453, <https://doi.org/10.1039/D3EE03073C>.
- [38] Y. Yue, Z. Jia, Y. Li, Y. Wen, Q. Lei, Q. Duan, J. Sun, Q. Wang, Thermal runaway hazards comparison between sodium-ion and lithium-ion batteries using accelerating rate calorimetry, *Process Saf. Environ. Prot.* 189 (2024) 61–70, <https://doi.org/10.1016/j.psep.2024.06.032>.
- [39] X. Liu, D. Ren, H. Hsu, X. Feng, G.-L. Xu, M. Zhuang, H. Gao, L. Lu, X. Han, Z. Chu, J. Li, X. He, K. Amine, M. Ouyang, Thermal Runaway of Lithium-Ion Batteries without Internal Short Circuit, *Joule* 2 (2018) 2047–2064, <https://doi.org/10.1016/j.joule.2018.06.015>.
- [40] D. Velumani, A. Bansal, Thermal Behavior of Lithium- and Sodium-Ion Batteries: A Review on Heat Generation, Battery Degradation, Thermal Runaway – Perspective and Future Directions, *Energy Fuels* 36 (2022) 14000–14029, <https://doi.org/10.1021/acs.energyfuels.2c02889>.
- [41] D. Ren, X. Feng, L. Liu, H. Hsu, L. Lu, L. Wang, X. He, M. Ouyang, Investigating the relationship between internal short circuit and thermal runaway of lithium-ion batteries under thermal abuse condition, *Energy Storage Mater.* 34 (2021) 563–573, <https://doi.org/10.1016/j.ensm.2020.10.020>.
- [42] X. Feng, M. Ouyang, X. Liu, L. Lu, Y. Xia, X. He, Thermal runaway mechanism of lithium ion battery for electric vehicles: A review, *Energy Storage Mater.* 10 (2018) 246–267, <https://doi.org/10.1016/j.ensm.2017.05.013>.
- [43] Y. Ding, Y. Li, R. Xu, X. Han, K. Huang, X. Ke, B. Wang, M. Sui, P. Yan, Cross-scale deciphering thermal failure process of Ni-rich layered cathode, *Nano Energy* 126 (2024) 109685, <https://doi.org/10.1016/j.nanoen.2024.109685>.
- [44] Y. Wang, X. Feng, Y. Peng, F. Zhang, D. Ren, X. Liu, L. Lu, Y. Nitta, L. Wang, M. Ouyang, Reductive gas manipulation at early self-heating stage enables controllable battery thermal failure, *Joule* 6 (2022) 2810–2820, <https://doi.org/10.1016/j.joule.2022.10.010>.
- [45] H. Che, S. Chen, Y. Xie, H. Wang, K. Amine, X.-Z. Liao, Z.-F. Ma, Electrolyte design strategies and research progress for room-temperature sodium-ion batteries, *Energy Environ. Sci.* 10 (2017) 1075–1101, <https://doi.org/10.1039/C7EE00524E>.